

## Study on 3D Unsteady Swirling Recirculating Flow in a Nozzle with a Slotted-tube

Hui-Fen Guo<sup>1,2</sup>, Bin-Gang Xu<sup>1,3</sup> and Sheng-Yan Li<sup>1</sup> and Chong-Wen Yu<sup>2</sup>

**Abstract:** Three-dimensional transient simulation is presented for swirling recirculating flow in a nozzle with a slotted-tube (different grooves) and the effect of the groove number is also investigated. The numerical results on the streamline angles are validated by experimental visualization using the surface oil flow technology. In the downstream center of the injectors, the vortex breakdown experiences a transition from bubble- to spiral- breakdown as time is increased. For all cases under study, as the sizes of two recirculation zones near the injector upstream wall and the step retain almost constant, the spiral breakdown shows a periodic development. The more the groove number is, the longer the computing time is to reach a periodic solution. For the case with four grooves, due to geometry symmetry, the vortex breakdown occurs earlier with axis, and the size and strength of the vortices are larger compared with that in two other cases with three and five grooves. Different from the results of the four grooves, which the breakdown point moves downward over time, the breakdown position is almost fixed for three and five grooves.

**Keywords:** Swirling flow, Vortex breakdown, Recirculation zone, Groove, Streamline angle

### 1 Introduction

Swirling flows have been applied in a wide range of engineering devices, such as cyclones, separators, combustions, and gas turbines, etc. In the 1960s, turbulent swirling decaying flow was applied to produce air-jet spun yarns. In this spinning system, the forming yarn is 'twisted' by operating two swirling air currents in mutually opposite directions in two successive nozzles. To improve resultant yarn quality, a slotted-tube (with rectangular grooves) is configured behind the first nozzle.

---

<sup>1</sup> Institute of Textiles and Clothing, the Hong Kong Polytechnic University, Kowloon, Hong Kong

<sup>2</sup> College of Textile, Donghua University, Shanghai 201620, China

<sup>3</sup> Corresponding author, E-mail: tcxubg@inet.polyu.edu.hk

zle (Fig. 1). Hence, a turbulent swirling recirculating flow in the nozzle with the slotted-tube is formed by tangentially injecting high-velocity compressed air into the twisting chamber through evenly spaced injectors from the air reservoirs (Fig. 1). Due to the effects of this swirling flow, fibers are displaced and rotated around other fibers that surround them, resulting in fiber twisting and wrapping around the neighboring fibers. Again, some factors in the swirling recirculating flow, such as the formation of the corner recirculation zone (CRZ), the occurrence of the vortex breakdown and its natural flow fluctuation (i.e., vortex breakdown point oscillation) will loose the fiber bundles and produce more wrapping fibers. All the above factors will help to produce a high quality yarn with good tensile strength. Therefore, the study on the flow characteristics of the unsteady swirling recirculating flow is of both theoretical and practical importance.

In numerical predictions, many studies have shown that the standard  $k$ - $\epsilon$  turbulence model (KEM) in general performs poor due to the neglect of both anisotropic viscosity and additional turbulence generation arising from the effects of streamline curvature [Nallasamy (1987)]. To simulate confined swirling flow, various adjustments and tuning to the KEM have been proposed [Kim and Chung (1987); Chang and Chen (1993)]. However, none of the existing modified KEMs were reported to be able to yield satisfactory predictions of swirling flows with the swirl intensities ranging from low to high extents. For example, Chang and Chen (1993) found that the hybrid KEM does not capture the off-axis tendency of the internal recirculation zones (IRZ) and yield poor predictions of the tangential velocity for much highly swirl level. For these much highly anisotropic flows, the Reynolds stress model (RSM) has been demonstrated to be capable of reproducing, to a certain extent, the major features of the flows such as the mean velocity profiles [Hogg and Leschziner (1989); Sharif and Wong (1995)]. However, the RSM over- or under-predicted turbulent stresses [Hogg and Leschziner (1989); Sharif and Wong (1995)]. Recently, Benim and Nahavandi (2003) has demonstrated that the steady RSM can lead to serious errors for some highly swirling turbulent flows, because the RSM cannot adequately represent the low frequency unsteady motion of coherent structures, which can play an important role in turbulent swirling flows. Therefore, the 3D unsteady RSM was proposed to investigate the swirling flow, and both the radial extension and closing shape of the IRZ can be quite well predicted [Benim, Nahavandi, Syed (2005)]. In the last few years, both large eddy simulation (LES) and direct numerical simulation (DNS) have also been used to predict swirling flows by several authors [Wang, Bai, Wessman (2004); Freitag M, Klein (2005)]. They are confirmed that the computational results are qualitatively in good agreement with the experimental ones. However, to date, DNS and LES simulations utilizing spectral schemes have been limited primarily to geometrically simple configurations,

and, for the case of DNS, the restrictions include relatively low Reynolds numbers. Despite the advances in modeling turbulent flow, the KEMs are still commonly used in the prediction of turbulent swirling flow. Nagendra (2001) has demonstrated that the realizable KEM [Shih, Liou, Shabbir, Zhu (1995)] is good in predicting the mean flow, especially in the downstream region and in the near axis region. The realizable KEM consists of a new model dissipation rate equation and a new realizable eddy viscosity formulation. It has shown substantial improvements on the standard KEM where the flow features include strong streamline curvature, vortices and recirculation. With such a background and engineering application, the present model has also adopted the realizable KEM for the solution of turbulent swirling circulating flows.

For a swirling flow, what parameter to use to characterize the swirl strength is very important. Several different formulations on the swirl intensity have been defined by many researchers. Escudier and Keller (1985) proposed a parameter, which was defined as the ratio of the azimuthal to the axial velocity components at the surface of the central cylinder within the annular cylindrical section and independent of the Reynolds number. The more commonly used parameter for most researchers is the swirl number  $S_n$ , which is the ratio of the axial flux of the angular momentum to the axial flux of the axial momentum [Gupta, Lilley, Syred (1984)]:

$$S_n = \frac{\int_0^{2\pi} \int_0^R u_z u_\varphi r^2 dr d\varphi}{R \int_0^{2\pi} \int_0^R u_z^2 r dr d\varphi} \tag{1}$$

where  $R$  is the tube radius,  $u_z$  is the mean axial velocity component,  $u_\varphi$ , the tangential one, and  $r$  and  $\varphi$  are radial and angular coordinates referred to tube center, respectively.

In the literature other swirl intensity definitions can also be found. Another important definition of swirl intensity is based on the streamline (swirl) angle [Yajnik and Subbaiah (1973)]:

$$\theta = \arctan(u_\varphi/u_z) \tag{2}$$

The swirl angles were evaluated at some position in the cross-section, such as, at  $r/R = \pm 0.6$  by at  $r/R = \pm 0.95$  by Yajnik and Subbaiah (1973) using probes, at  $r/R = \pm 0.50$  and  $\pm 0.91$  by Steenbergen and Voskamp (1998) with laser Doppler velocimeter (LDV), and at the wall by means of deposited oil traces by Sparrow and Chaboki (1984) and Chang (2004). These studies indicated the swirl angle is a function of a radial position.

Unlike the swirl number  $S_n$ , an axial change of the swirl angle is not caused by swirl decay only, but also by axial changes in the axial flow field. As pointed

out by Sparrow and Chaboki (1984), the swirl angle at any axial station can be characterized by the ratio of the tangential and axial shear stresses at the tube wall. Hence, on approaching the wall, the local swirl angle (*i.e.*, the wall swirl angle), which is the angle between the pipe axis and the mean flow direction, is defined as [Steenbergen (1995); Steenbergen and Voskamp (1998)]:

$$\tan \theta_{wall} = \lim_{r \rightarrow R} (u_\phi / u_z) = \frac{\tau_{\phi,wall}}{\tau_{z,wall}} \quad (3)$$

Ignoring the effects of the turbulent and viscous shear stresses and pressure, the tangential  $\tau_{\phi,wall}$  and axial  $\tau_{z,wall}$  wall shear stresses can be obtained (a detail derivation on these wall shear stresses can be found in ref. [Steenbergen (1995)]):

$$\tau_{\phi,wall} = \frac{\rho}{R^2} \frac{\partial}{\partial z} \int_0^R r^2 u_\phi u_z dr \quad \tau_{z,wall} = \rho \frac{\partial}{\partial z} \int_0^R r u_z^2 dr \quad (4)$$

Hence, near the wall the swirl angle is related to the rate of decay of the swirl. Furthermore, since swirl also increases the level of the axial wall shear stress [Kitoh (1991)], both the numerator and the denominator of Eq. (3) are a function of swirl number  $S_n$ . For example, Kitoh (1991) suggests to express  $\tau_{\phi,wall}$  as a series expansion in terms of  $S_n$ . For low swirl numbers one can decide to only retain the linear term, *i.e.*  $\tau_{\phi,wall} \sim S_n$ .

For air-jet spinning, axial velocity generates a suction to draw the fibers or strands into the nozzle and transfers them toward the nozzle outlet, while tangential velocity is responsible for twisting. Hence, the relation between the axial and tangential velocities, *viz.* a streamline angle plays an important role in yarn formation.

Based on the above, the present work aims to report some important aspects of 3D transient swirling recirculating flow in the nozzle with the slotted-tube and to discuss the effect of groove number on fluid flow, since the effects of the groove geometrical parameters on steady flow fields and yarn properties has been studied in our earlier work [Guo, Chen and Yu (2010)]. In addition, the streamline angle is measured in this paper using the surface oil flow (wall) visualization technology to demonstrate the validity of the proposed numerical method.

## 2 Numerical Model

### 2.1 Nozzle Structure

Normally a nozzle is made in a cylindrical shape and a slotted-tube with two to five rectangular- grooves is configured behind this nozzle in spinning process. Fig. 1 shows a 3D profile of the nozzle with four rectangular grooves. The origin of the Cartesian coordinates system is located at the center of the nozzle inlet. The  $z$ -axis

is taken as the stream-wise direction and the  $x - y$  plane is perpendicular to the  $z$ -axis (*i.e.* the nozzle inlet). For all cases under study, the twisting chamber diameter  $D$  is 2mm, the nozzle length  $L$  is 33mm, the diameter of the injector  $d$  is 0.45mm, the injection angle  $\beta$  is  $45^\circ$ , and the position of the injector  $l_1$ , which is the distance from the injector to the inlet, is 11mm. The groove's length  $l_2$ , depth  $h$  and width  $w$  are 8mm, 0.8mm and 0.3mm, respectively. Since groove number is an important parameter in determining yarn quality in air-jet spinning, the swirling with three different rectangular groove number— $n=3, 4, 5$ , which correspond to Case 1 to 3 respectively, are calculated.

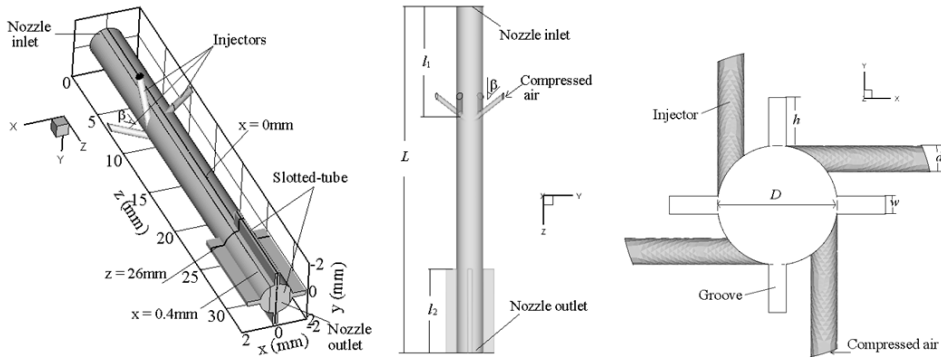


Figure 1: Geometrical profiles of a 3D model and projections of the nozzle with a slotted-tube (four- rectangular- groove)

## 2.2 Governing equations and turbulence model

In our simulation, the air entering the twisting chamber is modeled as a gas (air) in the absence of body forces. The fluid density obeys the ideal gas law and its viscosity, the specific heat capacity, and thermal conductivity are assumed to be constant. For compressible flows, Favre-averaged mean equations of continuity, the motion equation, the energy equation and the equation of state in Cartesian tensor notation can be written as follows [Favre (1969)]:

$$\frac{\partial \bar{\rho}}{\partial t} + \frac{\partial}{\partial x_i} (\bar{\rho} \tilde{u}_i) = 0 \quad (5)$$

$$\frac{\partial}{\partial t} (\bar{\rho} \tilde{u}_i) + \frac{\partial}{\partial x_j} (\bar{\rho} \tilde{u}_i \tilde{u}_j) = -\frac{\partial \bar{p}}{\partial x_i} + \frac{\partial}{\partial x_j} (\tilde{\tau}_{ij} - \overline{\rho u_i'' u_j''}) \quad (6)$$

$$\frac{\partial}{\partial t} (\bar{\rho} \tilde{e}) + \frac{\partial}{\partial x_j} (\bar{\rho} \tilde{u}_j \tilde{e}) = -\frac{\partial}{\partial x_j} [\tilde{u}_j \bar{p} + \tilde{u}_i (\overline{\rho u_i'' u_j''} - \tilde{\tau}_{ij})] + C_p (\overline{\rho u_j'' T} - \frac{\mu}{Pr} \frac{\partial \tilde{T}}{\partial x_j}) \quad (7)$$

where an overbar indicates the mean with Reynolds averaging. A tilde and a double prime are corresponding to ones for Favre averaging. Also,  $x_i$  ( $i = x, y, z$ ) are the coordinate directions in Cartesian coordinates, and  $u_i$  are the velocities in the three coordinates directions.  $\rho$ ,  $p$ ,  $T$ ,  $\mu$  and  $Pr$  are the air density, pressure, temperature, laminar viscosity and Prandtl number, respectively.  $k$  defined by  $\bar{\rho}k = \frac{1}{2}\overline{\rho u_i'' u_i''}$  is the turbulence kinetic energy,  $\bar{e}$  is the mean total energy and  $\gamma$  is the ratio of specific heats.  $\bar{t}\tilde{a}u_{ij}$  is the mean viscous stress tensor.

In the present study, the realizable KEM [Shih, Liou, Shabbir, Zhu (1995)] is adopted to close Favre- averaged equations. The modeled transport equations for  $k$  and  $\varepsilon$  are:

$$\frac{\partial \bar{\rho}k}{\partial t} + \frac{\partial}{\partial x_i}(\bar{\rho}\tilde{u}_i k) = \frac{\partial}{\partial x_i}[(\mu + \frac{\mu_t}{\sigma_k})\frac{\partial k}{\partial x_j}] + G_k - \bar{\rho}\varepsilon - Y_M \quad (8)$$

and

$$\frac{\partial(\bar{\rho}\varepsilon)}{\partial t} + \frac{\partial}{\partial x_i}(\bar{\rho}\tilde{u}_i \varepsilon) = \frac{\partial}{\partial x_i}[(\mu + \frac{\mu_t}{\sigma_\varepsilon})\frac{\partial \varepsilon}{\partial x_j}] + \bar{\rho}C_1 S \varepsilon - \bar{\rho}C_2 \frac{\partial^2}{k + \sqrt{\mu\varepsilon}} \quad (9)$$

where  $\mu_t$  is a turbulent viscosity.  $C_1 = \max [0.43, \eta/(\eta+5)]$  and  $\eta = Sk/\varepsilon$ .  $\sigma_k$  and  $\sigma_\varepsilon$  are the turbulent Prandtl numbers for  $k$  and  $\varepsilon$ , respectively. The constants used in this model are defined:  $C_2=1.9$ ,  $\sigma_k=1.0$ ,  $\sigma_\varepsilon=1.2$ .  $S$  is the modulus of the mean rate-of-strain tensor  $S_{ij}$ , defined as

$$S \equiv \sqrt{2S_{ij}S_{ij}} \quad S_{ij} = \frac{1}{2}\left(\frac{\partial \tilde{u}_j}{\partial x_i} + \frac{\partial \tilde{u}_i}{\partial x_j}\right) \quad (10)$$

$G_k$  represents the generation of turbulence kinetic energy due to the mean velocity gradients. With the Boussinesq hypothesis, it is described as

$$G_k = \mu_t S^2 \quad (11)$$

The fluctuating dilatation dissipation term in compressible turbulence,  $Y_M$ , is modeled as

$$Y_M = 2\bar{\rho}\varepsilon \frac{k}{a^2} \quad (12)$$

Here  $a$  is the speed of sound.

### 2.3 Boundary conditions

Boundary conditions are required for all boundaries of the computational domain. At the injector inlet, because the pressure of the air reservoir is known, pressure inlet condition is specified as total pressure  $P_t$ , static pressure  $P_s$  and static temperature  $T_{in}$ . The other inlet flow parameters such as Mach number  $M_{in}$ , velocity  $V_{in}$ , density  $\rho_{in}$ , turbulence kinetic energy  $k_{in}$  and turbulence dissipation  $\varepsilon_{in}$  can be calculated at the following conditions:

$$\begin{aligned}
 M_{in} &= \sqrt{2[(P_t/P_s)^{(\gamma-1)/\gamma} - 1]/(\gamma - 1)} \\
 \mathbf{V}_{in} &= M_{in}\sqrt{\gamma R_c T_{in}} \quad \rho_{in} = P_t/(R_c T_{in}) \\
 k_{in} &= (0.07v_{in})^2 \quad \varepsilon_{in} = C_\mu k_{in}^{1.5}/(0.07d)
 \end{aligned}
 \tag{13}$$

where  $R_c$  and  $C_\mu$  are gas constant and empirical constant, respectively.

At the nozzle inlet, while the fibers or strands output from the front roller and go into the nozzle, the outer air is supplied into the nozzle. The airflow velocity (which is only 1-3 m/s) is largely smaller than that at the injector inlet. However, due to compressible flow at the injector inlet, to avoid a nonphysical result using the velocity inlet condition, pressure inlet condition is also set at the nozzle inlet.

Due to the pressure inlets and compressible flow, the pressure outlet conditions at the nozzle outlet are specified with a static pressure and a set of backflow conditions. The backflow conditions will be used if the flow reverses direction at the pressure outlet boundary during the solution process.

At the wall, no-slip boundary conditions are applied.

### 2.4 Numerical method

Eqs. (5)- (9) can be recast in a general form (For simplicity we shall omit the overbar denoting the Reynolds and Favre average.):

$$\frac{\partial \rho \varphi}{\partial t} + \text{div}(\rho \mathbf{V} \varphi) = \text{div}(\Gamma \text{grad} \varphi) = S_\varphi
 \tag{14}$$

Here  $\varphi$  is a general variable,  $\Gamma$  a diffusion coefficient, and  $S_\varphi$  a general source term. The vector represents the fluid velocity.

The governing equations are discretized on a block-structured collocated grid following the finite-volume approach based on the FLUENT code. Discretization of on an arbitrary control volume or cell  $V$  may be written as

$$\sum_f^{N_f} \rho_f V_f \varphi_f \cdot A_f - \sum_f^{N_f} \Gamma_\varphi (\nabla \varphi)_n \cdot A_f = S_\varphi V
 \tag{15}$$

where  $N_f$  is number of faces enclosing cell,  $\varphi_f$ , are the values of  $\rho$  and  $\varphi$  through face  $f$ , respectively.  $A_f$  is area of face  $f$ ,  $|\nabla\varphi|$  is magnitude of  $\nabla\varphi$  normal to face  $f$ .

Due to compressible effects, the density-based (implicit) approach is adopted. The density-based method solves the governing equations of continuity, momentum, and energy simultaneously as a set of equations, and the equations for additional scalars will be solved sequentially (i.e., segregated from one another and from the coupled set). To reduce the numerical diffusion in low-order schemes, high-order accurate schemes are employed here. For the conservation equations, the second-order upwind (SOU) schemes are applied, the face value  $\varphi_f$  is computed:

$$\varphi_f = \varphi_u + \nabla\varphi_u \cdot \Delta\vec{s} \quad (16)$$

where  $\varphi_u$  and  $\nabla\varphi_u$  are the cell-centered value and its gradient in the upstream cell, and  $\Delta\vec{s}$  is the displacement vector from the upstream cell centroid to the face centroid.

A previous study [Shore, Haynes, Fletcher and Sola (1996)] indicated that the generalized QUICK scheme is superior to other schemes for swirling flows. For a regularly spaced grid, the generalized quadratic upstream interpolation of convective kinematics (QUICK) scheme [Leonard and Mokhtari (1990)] is of third-order accuracy, and for an irregularly spaced grid, the scheme is of second-order accuracy. Hence, the  $k$  and  $\varepsilon$  equations are solved using QUICK scheme. For the cell 'e' with centre  $E$ , the general QUICK expression yields:

$$\varphi_e = \theta \left[ \frac{s_e}{s_p + s_e} \varphi_p + \frac{s_p}{s_p + s_e} \varphi_E \right] + (1 - \theta) \left[ \frac{s_w + 2s_p}{s_p + s_w} \varphi_p - \frac{s_p}{s_p + s_w} \varphi_w \right] \quad (17)$$

Here points  $W$  and  $P$  are two points upstream of the point  $E$ .  $s_w$ ,  $s_p$  and  $s_e$  are the lengths of the corresponding control volume of points  $W$ ,  $P$  and  $E$ , respectively.

The realizable KEM is primarily valid for fully developed turbulent flows. Consideration therefore needs to be given of how to make these models suitable for near-wall flows. Many studies have shown that the KEMs with non-equilibrium wall functions [Kim and Choudhury (1995)] can provide the best predictions for complex flows [Kim, Ghaja, Tang and Foutch (2005)]. The non-equilibrium functions assume that the wall-neighbouring cells consist of a viscous sub-layer and a fully turbulent layer and need to resolve the  $k$  equation at the wall-neighbouring cells. It partly account for the effects of pressure gradients and departure from equilibrium. Thus, a non-equilibrium wall function is adopted here. The log-law for mean velocity sensitized to pressure gradients is:

$$\frac{\tilde{U} C_\mu^{1/4} k^{1/2}}{\tau_w / \rho} = \frac{1}{\kappa} \ln \left( E \frac{\partial C_\mu^{1/4} k^{1/2} y}{\mu} \right) \quad (18)$$

where

$$\tilde{U} = U_P - \frac{1}{2} \frac{dp}{dx} \left[ \frac{y_v}{\rho \kappa \sqrt{k}} \ln\left(\frac{y}{y_v}\right) + \frac{y - y_v}{\rho \kappa \sqrt{k}} + \frac{y_v^2}{\mu} \right] \quad (19)$$

$$y_v = \frac{\mu y_v^*}{\rho C_\mu^{1/4} k_P^{1/2}} \quad (20)$$

and  $\kappa=0.4187$  is the von Karman constant,  $U_P$  and  $k_P$  represent the mean velocity of the fluid and turbulent kinetic energy at point  $P$ , respectively.  $E=9.793$  is an empirical constant,  $y_v$  is physical viscous sub-layer thickness, and . Thus the profile assumption made for turbulence quantities are:

$$\tau_t = \begin{cases} 0, & y < y_v \\ \tau_w, & y > y_v \end{cases} \quad k = \begin{cases} \left(\frac{y}{y_v}\right)^2 k_P, & y < y_v \\ k_P, & y > y_v \end{cases} \quad \varepsilon = \begin{cases} \frac{2\nu k}{y^2}, & y < y_v \\ \frac{k^3/2}{C_l y}, & y > y_v \end{cases} \quad (21)$$

where  $C_l = \kappa C_\mu^{-3/4}$  and  $\nu$  is kinematic viscosity.

### 3 Experimental

To prove validation of the numerical code, the streamline angle is measured using the surface oil flow technology. As described in Section 2.1, the model used for the experiments has been enlarged in size because the actual model is too small. In air-jet spinning process, the only predominant force acting on the fibers is the drag force. Drag force in general is a function of Reynolds number (Re) and Mach number (M). Therefore, any dynamic similarity will result from the similarity of friction force the force stemming from the compressibility of the fluid, characterized by:

$$Re_p = \frac{\rho_p \mathbf{V}_p D_p}{\mu_p} = \frac{\rho_m \mathbf{V}_m D_m}{\mu_m} = Re_m \quad (22)$$

$$M_p = \frac{\mathbf{V}_p}{\mathbf{a}_p} = \frac{\mathbf{V}_m}{\mathbf{a}_m} = M_m \quad (23)$$

where the subscripts  $p$  and  $m$  denote the prototype and model, respectively.  $V$  and  $a$  are the flow velocity and acoustic speed, respectively. The Mach number is important in high-speed compressible flows like that in air-jet spinning nozzle where density variations become significant. In such case, the equality of Mach numbers needs to be considered for dynamically similar modeling of this high-speed compressible flow from the spinning nozzle.

Since air under room temperature is working fluid for both the prototype and model, acoustic speeds for the two systems must be the same for the same operating pressures at room temperature, i.e.,  $a_p = a_m$  and  $V_p = V_m$ . A geometrically similar

model is therefore also dynamically similar to prototype when they operate at the same pressure. Here a length-scaling factor of 6 was chosen as a compromise between the need to keep the compressed-air consumption rate below the level that can be delivered by the installed compressor and the desire for a reasonably large model in order to measure conveniently.

Fig. 2 shows an experimental setup that is used to study the streamline angle in the tangentially injected swirling flow in a nozzle. The compressed air from a compressor is pumped into the nozzle through the injectors. Before the air gets bifurcated into the tangential injectors, it is made to pass through a flowmeter where the total flow into the nozzle is recorded. The four branches of the injectors are also fitted with four bourdon type pressure gauges to know the inlet pressure at the entrance to the injectors. The nozzle is made of plexiglass tube. The inner surface of the nozzle is coated with a mixture of carbon powder and silicon oil. To eliminate parallax induced by curved surface in the photography, a method proposed by Settles and Teng (1983) is adopted: the remained carbon power over the surface is removed using self-adhering contact paper. The angle made by the flow relative to the tube axis can be measured.

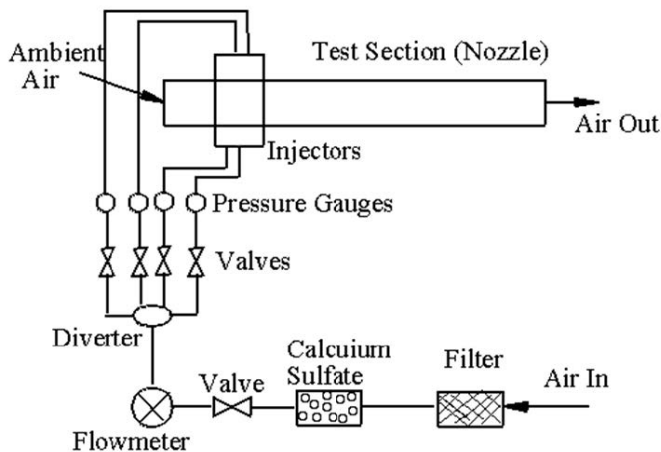


Figure 2: Schematic diagram of experimental apparatus

## 4 Results and discussion

### 4.1 Grid independency

The physical domain for the present solution has already been described in Section 2.1. Due to the sharp-pointed angles, located in the intersection between the injec-

tors and the twisting chamber, a hybrid non-uniform grid is generated (Figure 3). In all cases, grid refinements in the regions of expected high gradients, e.g., near the wall and at the zone corresponding to the intersection volume between the injectors and the twisting chamber, are applied. One constraint of the grid generation is the position of the first elementary volume closest to the wall. A criterion  $y^+ \equiv \rho u_\tau y / \mu$  is usually defined to characterize this cell location in wall-coordinate. Here  $u_\tau$  is the friction velocity and  $y$  is the normal distance from the center of the cell to the wall. With application of a non-equilibrium wall-function based on the universal logarithmic profile, each wall-adjacent cell's centroid should be located within the log-law layer. A  $y^+$  value is set close to  $y^+ = 30$  [Launder and Spalding (1974)].

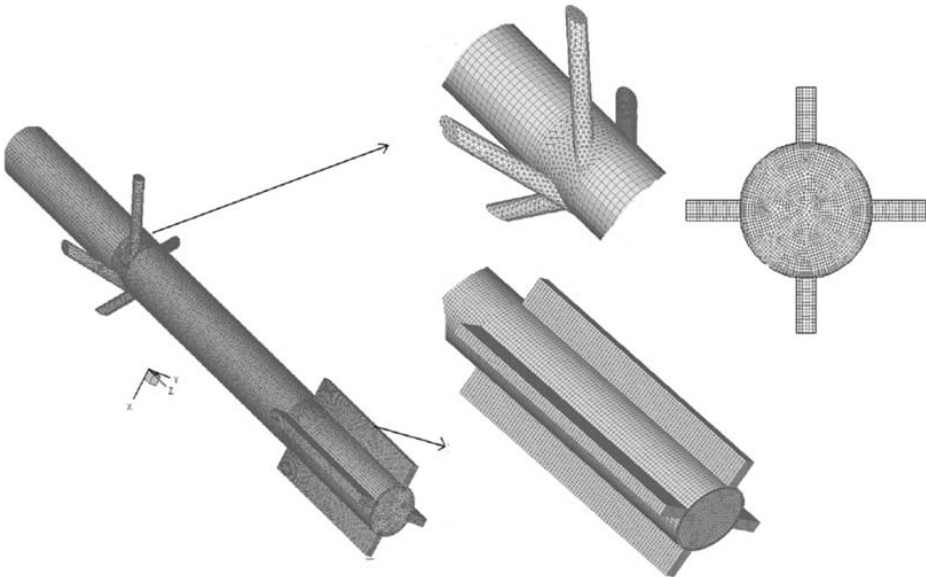


Figure 3: Mesh topology of the nozzle with a four-rectangular-groove slotted-tube (Case 2).

Three different grids with 166 766 (Grid 1), 218 844 (Grid 2) and 268 795 (Grid 3) cells for a nozzle with a four-rectangular-groove (Case 3) are used in the calculation in order to check the independence of the solutions on the grid. Figure 4 shows the variations of the mean axial and tangential velocity components near the injectors outlet (i.e.  $z=12\text{mm}$ ) for steady swirling flow. As seen, all three grids predict similar velocity profiles. Therefore, the mesh employed will be deemed to be satisfactory and further refinements of the mesh will not be beneficial. Considering the computational effort, Grid 2 is adopted for this case (four-rectangular-groove). Sev-

eral computational trials are also run with various grid resolutions for other cases (nozzles with 3 and 5 rectangular-groove, respectively). It will not be described here.

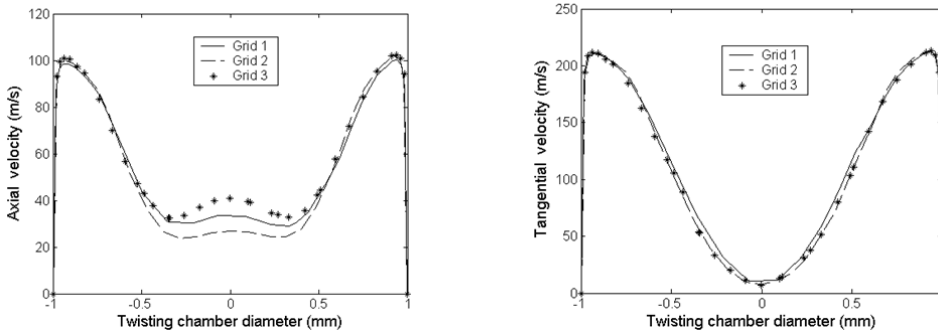


Figure 4: Comparison of mean velocity profiles at axial position  $z=12\text{mm}$  with various mesh configurations for a nozzle with a four-rectangular-groove (Case 2).

#### 4.2 Validation of the numerical code

The swirling flow field induced by tangential inlets is strongly dependent on the initial swirl intensity. Because these velocities in Eq. (1) cannot be known a priori, a geometric swirl number  $S_g$  (*i.e.*, the local swirl intensity at the injection location) based on conservation of momentum can be adopted [Chang and Dhir (1994)]:

$$S_g = \left(\frac{m_t}{m_T}\right)^2 \left(\frac{D}{d}\right)^2 \frac{\sin \theta}{N} \quad (24)$$

where  $m_t$  and  $m_T$  are the total mass flow rates through the injectors and the test section, respectively.

Unless stated otherwise, the following conditions were used for all studied cases. At the injector inlet, the pressure is  $2.5 \times 10^5$  Pa. Hence, according to Eq. (13), the inlet Mach number  $M_{in}$  is 1.2, and as  $m_t/m_T = 1$  (Ignoring the effects of the airflow in the nozzle inlet), the initial swirl intensity  $S_g = 3.49$  with Eq. (24). However, the Reynolds number based on the injector velocity and the injector diameter is  $3.04 \times 10^4$  for simulation, and  $1.216 \times 10^5$  (the model is enlarged to 6 times) for experiment with Mach scale law (see also Section 3). The air velocity at the nozzle inlet for simulation and experiment are, respectively, 1 m/s and 0 m/s (*i.e.*, ambient air).

Due to the difficulty of groove manufacturing, only the streamline angle in a nozzle without slotted-tube (*i.e.*, a cylindrical tube) is experimentally observed. In order to

compare with the experimental data, the 3D steady swirling airflows are firstly calculated, and then the wall streamlines angles,  $\theta$ , with respect to the axis direction, are determined with Eq. (3). Besides the nozzle without a slotted-tube, the nozzle with a slotted-tube is also considered to illustrate the functions of the slotted-tube here. Noted that, for all the cases under study, the initial swirl numbers are the same with Eq. (24).

The computed streamline angles in the downstream of the injectors for the nozzle without slotted-tube are compared with the experimental results using the surface oil flow method (Fig. 5). In accordance with Sparrow and Chaboki (1984), the wall streamline angle decreases with increasing downstream distance due to the decay of the tangential wall shear. It is also observed from Fig. 5 that the model prediction differs from the experimental results in the quantitative sense. The delaying of the streamline angle with axis in experiment is faster than that in the simulation. As mentioned in Kitoh (1991), Steenbergen (1995) and Steenbergen and Voskamp (1998), the wall shear stresses for a incompressible confined swirling flow are a function of the Reynolds number  $Re$  and the swirl number  $S_n$ . Therefore, under the same initial swirl number (ignoring the effects of the airflow in the nozzle inlet), one reason of the discrepancies between numerical simulation and experiment maybe negligence of the effect of viscosity (i.e., Reynolds number), which only considers Mach similarity in the experimental study. In addition, the difference may be also attributed to the variation in inlet conditions. In the measurement, the supplement of air through the nozzle inlet, which will lead to change slightly in the initial swirl number and further the flow field, is ignored. It needs to be pointed out that far from the nozzle inlet, the effect of the discrepancy in the nozzle inlet is very weak. This is because the velocity in the nozzle inlet (1 m/s) is very smaller than that in the injector inlets (about 416 m/s with Eq. (13)). However, in a qualitative sense, the model predicts the streamline angle distributions quite well, as seen from the figure.

Comparison of the simulated streamline angles for the nozzles with and without the slotted-tube (Fig. 5) shows that the streamline angle in the nozzle with the slotting-tube is higher than that in the one without the slotting-tube, especially near the nozzle outlet. Thus, the twisting force acting on the fiber is increased due to the increase of the tangential velocity, and as a result, yarn tenacity is improved significantly for the nozzle with the slotted-tube. The functions of the slotted-tube can be demonstrated.

### **4.3 Transient flow structure**

To investigate the transient phenomena of flow structure in the nozzle with the slotted-tube, a swirling flow with an injector inlet pressure of  $P = 2.5 \times 10^5 \text{Pa}$  is

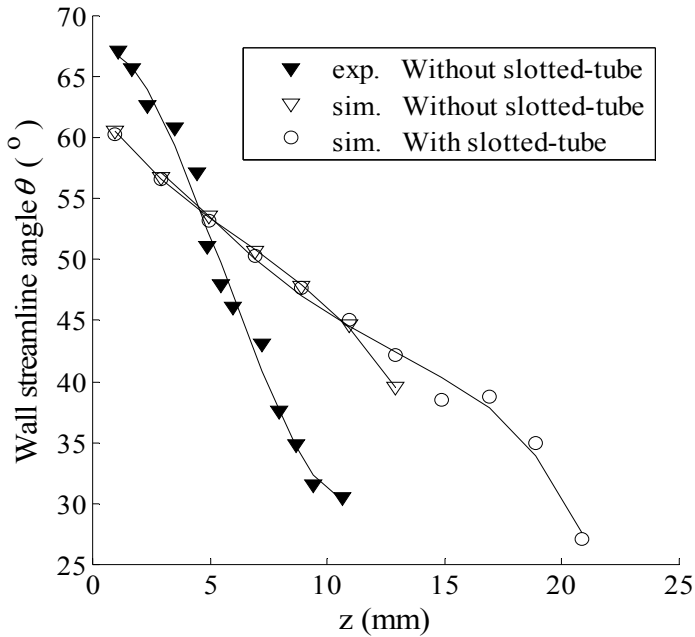


Figure 5: Comparison of the computed streamline angles in the injectors downstream of the nozzle with/without slotted-tube with the experimental results using surface oil flow method

computed. A time step of  $10^{-6}$ s was used for all the simulations, the number of iterations was fixed such that the solution converged in about 20 iterations for each time step. The flow field is initialized using a steady calculation, in which a global mass balance had been enforced and residuals of other variables had been considerably reduced. Convergence was judged not only by examining the scaled residual values (i.e., residual is normalized by the respective the largest absolute value of the residual in the first five iterations) for all solution variables, but also by monitoring the average value of mass-flow-rate on  $z=12$ mm and  $z=26$ mm surfaces.

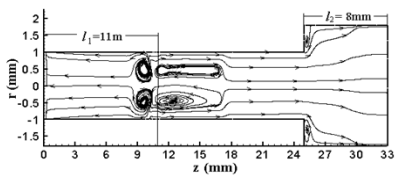
As an example, a series of time evolution flow structure with the computed streamlines in the  $y-z$  plane at  $x=0$ mm are described in this Section for the nozzle with four grooves (Case 2). As observed (Fig. 6), the swirling flow field experiences a complex flow process. In the upstream of the injectors, an interface between the inflow from the nozzle inlet and reverse-jet airflow of the injectors is formed (Fig. 6(a)). The location of the interface moves downstream gradually and finally disappears at  $t = 2.7 \times 10^{-4}$ s (Fig. 6(b-f)). The evolution of the interface is closely

related to the recirculation zones near the upstream wall of the injectors. At the initial time, a vortex ring can be observed due to the reverse jet. The vortex ring is stretched in the axial direction and a second vortex ring near the nozzle inlet is formed as time is increased (Fig. 6(a-d)). These vortex rings quickly change shapes and decay gradually with time, consequently, they diminish at  $t=2.7 \times 10^{-4}$ s (Fig. 6(f)), and then, a new vortex will be generated. Note that the flow state in upstream of the injectors keeps almost constant after  $t = 8.6 \times 10^{-4}$ s (Fig. 6(j-r)).

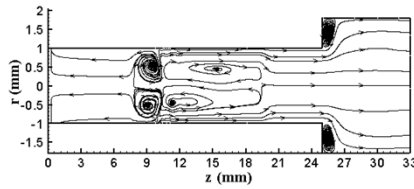
In the downstream of the injectors, the evolution of vortex breakdown is observed. At the initial time step, a bubble-type vortex breakdown is generated. Further, the size of the bubble is increased in the axial direction with time (Fig. 6(a-c)). As seen in Fig. 6, the distribution of circumferential vortices has an elliptic vortex-ring like structure that does not consist of closed circular vortex lines. At about  $t = 1.7 \times 10^{-4}$ s, internal structure of bubble shows approximately symmetric spiral-like vortices rotating in opposite directions that reveals a start of the transition from bubble- to spiral- breakdown (Fig. 6(d)). The vortex breakdown's development is in agreement with previous experiments by Sarpkaya (1971), Escudier (1988), and Brücker and Althaus (1995) who observed that the formation of an approximately axisymmetric vortex-ring-like structure stands for the bubble-type breakdown. After generation, the bubble showed a tendency to move upstream and to grow in size and later, in dependence on the initial flow conditions, to change to the spiral.

The location of the spiral-type vortex breakdown moves in downstream direction and gradually decreases in size (Fig. 6(e, f)). The vortex ring flow gradually diminishes when it gets into the slotted-tube (Fig. 6(g)). After that, the spiral shows the tendency to move upstream and to grow in size (Fig. 6(h, i)). After  $t = 8.6 \times 10^{-4}$ s, the flow obviously shows periodical decaying development (Fig. 6(j-r)), which is similar to the results of Brücker's observation [Brücker (1993)]. The breakdown point is about  $z = 15$  mm. In comparison to Fig. 6(j) the flow field looks turned around the centerline about  $180^\circ$  at the semiperiod in Fig. 6(l), where the breakdown point moves downstream slightly. First in Fig. 6(j), there are two clockwise vortices above the centerline. On the other side of the centerline, there are three counterclockwise rotating vortices on the left and right sides of two upper vortices. Above the centerline, the two vortices gradually incorporate and decrease; at the same time, two new clockwise vortices begin to grow near both the breakdown point and the nozzle outlet (Fig. 6(l)). The same process seems to take place below the centerline with a reversed sign of vorticity (Fig. 6(m-p)). As time is further increased (in a new period), owing to the decaying fluid, the location of vortex breakdown moves downward (around  $z = 18$  mm in Fig. 6(q) and (r)), and the strength and size of the vortices decrease (Fig. 6(q) and (r)).

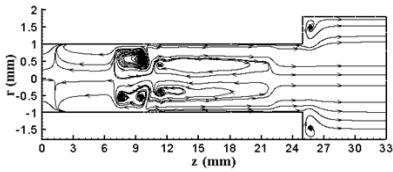
The corner recirculation zone (CRZ) is caused by the flow separation from the step



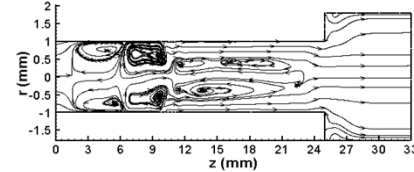
(a)



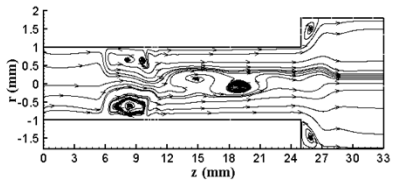
(b)



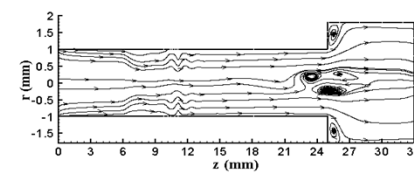
(c)



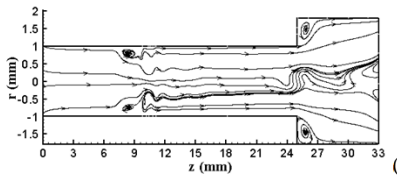
(d)



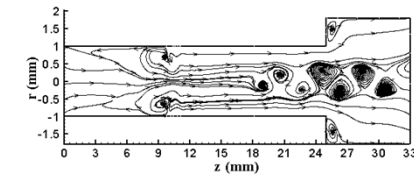
(e)



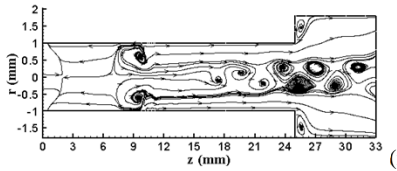
(f)



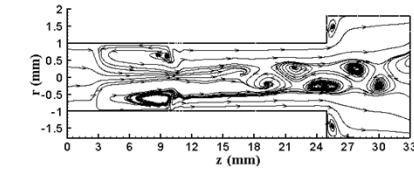
(g)



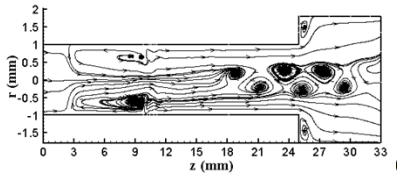
(h)



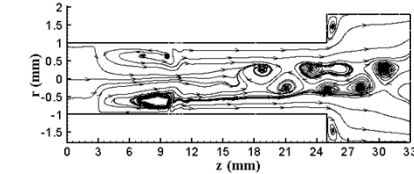
(i)



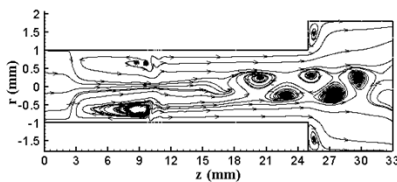
(j)



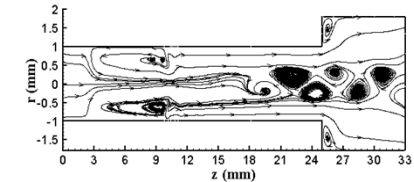
(k)



(l)



(m)



(n)

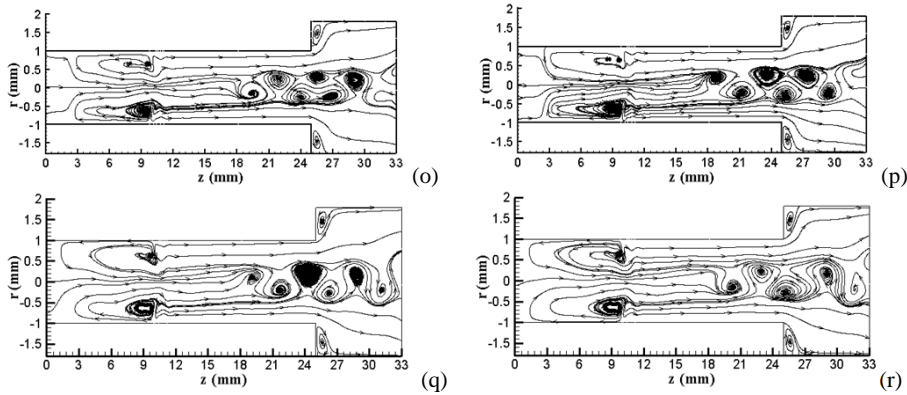


Figure 6: Time series of the streamlines in the  $y-z$  plane at  $x=0\text{mm}$  for a nozzle with four rectangular grooves (Case 2): (a)  $t=9.0\times 10^{-5}\text{s}$ ; (b)  $t=1.2\times 10^{-4}\text{s}$ ; (c)  $t=1.5\times 10^{-4}\text{s}$ ; (d)  $t=1.7\times 10^{-4}\text{s}$ ; (e)  $t=2.1\times 10^{-4}\text{s}$ ; (f)  $t=2.7\times 10^{-4}\text{s}$ ; (g)  $t=4.1\times 10^{-4}\text{s}$ ; (h)  $t=5.1\times 10^{-4}\text{s}$ ; (i)  $t=5.4\times 10^{-4}\text{s}$ ; (j)  $t=8.6\times 10^{-4}\text{s}$ ; (k)  $t=8.8\times 10^{-4}\text{s}$ ; (l)  $t=8.9\times 10^{-4}\text{s}$ ; (m)  $t=9.1\times 10^{-4}\text{s}$ ; (n)  $t=9.4\times 10^{-4}\text{s}$ ; (o)  $t=9.7\times 10^{-4}\text{s}$ ; (p)  $t=9.9\times 10^{-4}\text{s}$ ; (q)  $t=1.99\times 10^{-3}\text{s}$ ; (r)  $t=2.04\times 10^{-3}\text{s}$

of the groove as the fluid stream enters. It is observed from figures that the CRZ first increases then decreases, and disappears when bubble-type breakdown initiates the transition to a spiral-type one (Fig. 6(a-d)). After  $t=2.1\times 10^{-4}\text{s}$ , the size of CRZ keeps almost constant (Fig. 6(e-r)).

In accordance with our simulations, as the fiber strand passes through the twisting chamber, the weak opposite swirling balloon near the upstream wall can delay the edge fiber end to be picked up by the core strand and help to form a larger twist difference. Both the buffeting of vortex breakdown and the opposite winding of the spiral in spiral breakdown will help producing more wrapping fibers. Again, the vortices in the grooves will prolong the residence time of the fibers, which makes the fiber bundle looser. Hence, according to the principle of air-jet spinning, the preferred function of the slotted-tube can be demonstrated and yarn tenacity can be improved.

#### 4.4 The influence of the groove number

To illuminate the effect of the groove number, unsteady calculations of the other two cases with three and five grooves are carried out. Figs. 7 and 8 show the transient streamline patterns with the periodic changes of the vortex breakdown for two different groove number ( $n=3, 5$ ). Like the case with four grooves ( $n=4$ ),

as the sizes of both the CRZ behind the step of the groove and the recirculation zone in upstream of the injectors keeps almost constant, the vortex breakdown in the downstream of the injectors starts a periodic change. It is obvious from Figs. 6-9 that with the increasing of the groove number, the flow structure becomes more complex, and much longer computing time is needed to have a periodic solution. Again, since the vortex breakdown occurs earlier with axis and the geometry is symmetric, the size and strength of the vortices in case 2 ( $n=4$ ) are the largest compared with that in two other cases ( $n=3, 5$ ).

As is seen in Fig. 7, for  $n=3$  (case 1), the vortex breakdown first appears periodic change at about  $t=8.1 \times 10^{-4}$ s. During a period time, the number and the strength of the vortex rings first increase gradually (Fig. 7(b) and (c)) and then decrease (Fig. 7(d)) until a new period appears (Fig. 7(e)). With the increase of the time, however, the strength and size of the vortices in the new period decrease compared with that in previous periods (see also Fig. 7(a), (e) and (f)). Especially, as the time increased to a certain value ( $t=2.06 \times 10^{-3}$ s), it is difficult to form a vortex ring (Fig. 7(f)), though the position of the vortex breakdown is almost fixed (around  $z=17$  mm) in time. From all the figures, the flow structures in upstream of the injectors do not change much over time, which is similar to the case 2 ( $n=4$ ).

Compared with cases 1 and 2 ( $n=3, 4$ ), it needs much long time to reach a period solution for case 3 ( $n=5$ ). As shown in Fig.8, at the onset of the first period ( $t=1.1 \times 10^{-3}$ s), four vortices first appears above the centerline. These vortices quickly change shape with the first two vortices merging and the one near the nozzle outlet diminishing at  $t=1.13 \times 10^{-3}$ s (Fig. 8 (b)). Then, at  $t=1.15 \times 10^{-3}$ s, each one of above two vortices is split into two small vortices (Fig. 8 (c)). After that, the vortices merge again and a new vortex appears near the nozzle outlet and moves upward (Fig.8(c) and (d)). At about  $t=1.22 \times 10^{-3}$ s, a new period is generated (Fig.8(e)). It is also noted that the two small vortices below the centerline remain nearly unchanged during a periodic time. Comparison of Fig.8(a), (f) and (g) show that the strength of the vortices increase with time, especially a strong vortex under the centerline is formed near the nozzle outlet (see also Fig.8(h)). This contradicts the results of the cases 1 and 2 ( $n=3, 4$ ), which the fluid decays over time. Like case 2 ( $n=3$ ), the breakdown points seem to be “frozen” in at the same position (around  $z=18$ mm), as seen from Fig.8. Different from the case 2, however, the points depart from the centerline and are below the center axis.

To further illuminate the effect of the groove number, 3D steady swirling flows for three cases ( $n=3-5$ ) are also simulated using realizable KEMs here. Fig. 9 gives the results of the steady state streamlines at three sections for different groove number. As seen in Figs.6-9, there is obvious discrepancy for the flow structures which are calculates by the unsteady and steady realizable KEMs respectively. This agrees

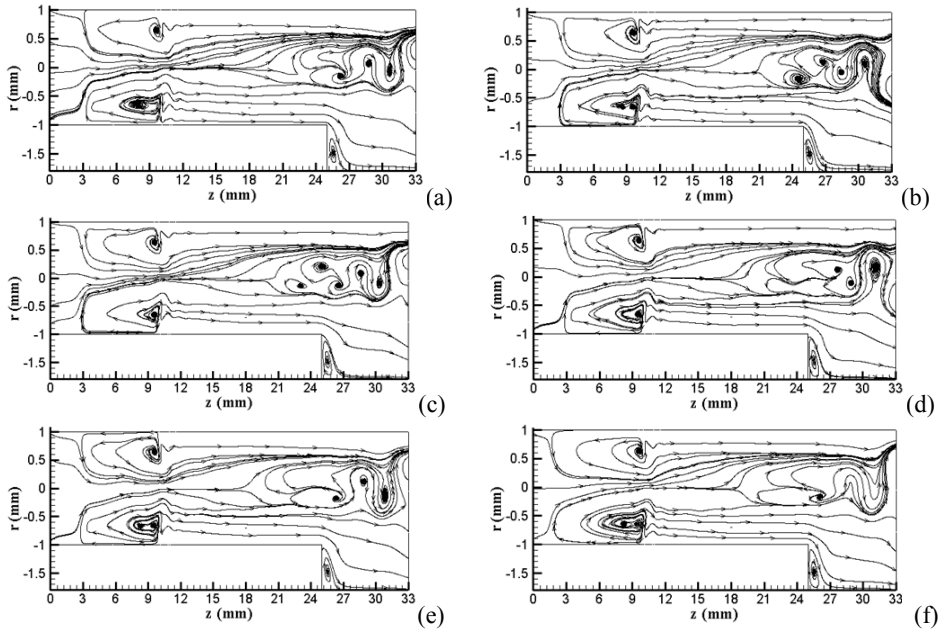


Figure 7: Time series of the streamlines in the  $y - z$  plane at  $x=0\text{mm}$  for a nozzle with three rectangular grooves (Case 1): (a)  $t=8.1 \times 10^{-4}\text{s}$ ; (b)  $t=8.3 \times 10^{-4}\text{s}$ ; (c)  $t=8.5 \times 10^{-4}\text{s}$ ; (d)  $t=8.8 \times 10^{-4}\text{s}$ ; (e)  $t=9.0 \times 10^{-4}\text{s}$ ; (f)  $t=2.06 \times 10^{-3}\text{s}$

with the results indicated by Benim and Nahavandi (2003) and Benim, Nahavandi and Syed (2005), who pointed out that steady RANS-based turbulence model can lead to serious errors for some highly swirling turbulent flows, because it cannot represent adequately the low frequency unsteady motion of coherent structures.

As shown in Fig.9, the recirculation zones near the upstream injector wall are generated due to a reverse jet for all cases. A central toroidal recirculation zone (CTRZ) in the downstream core region of the injectors is accompanied by a corner recirculation zone (CRZ), which is provoked by the sudden expansion in the flow field, i.e. a similar backward-facing step flow in the slotted-tube is generated due to the groove. These phenomena are in agreement with previous experiments [Dellenback, Metzger and Neitzel (1988); Nejad and Ahmed (1992)]. It is also noted that spiral-type vortex breakdown is generated in the CTRZ. As groove number  $n < 4$ , the location of the breakdown point moves in the upstream direction. While  $n = 5$  (case 3), the recirculation zone in the downstream of the injectors decreases quickly. For the recirculation zones in the upstream of the injectors, it is larger in the nozzle with even groove number ( $n=4$ ) than that in the nozzle with the odd groove number

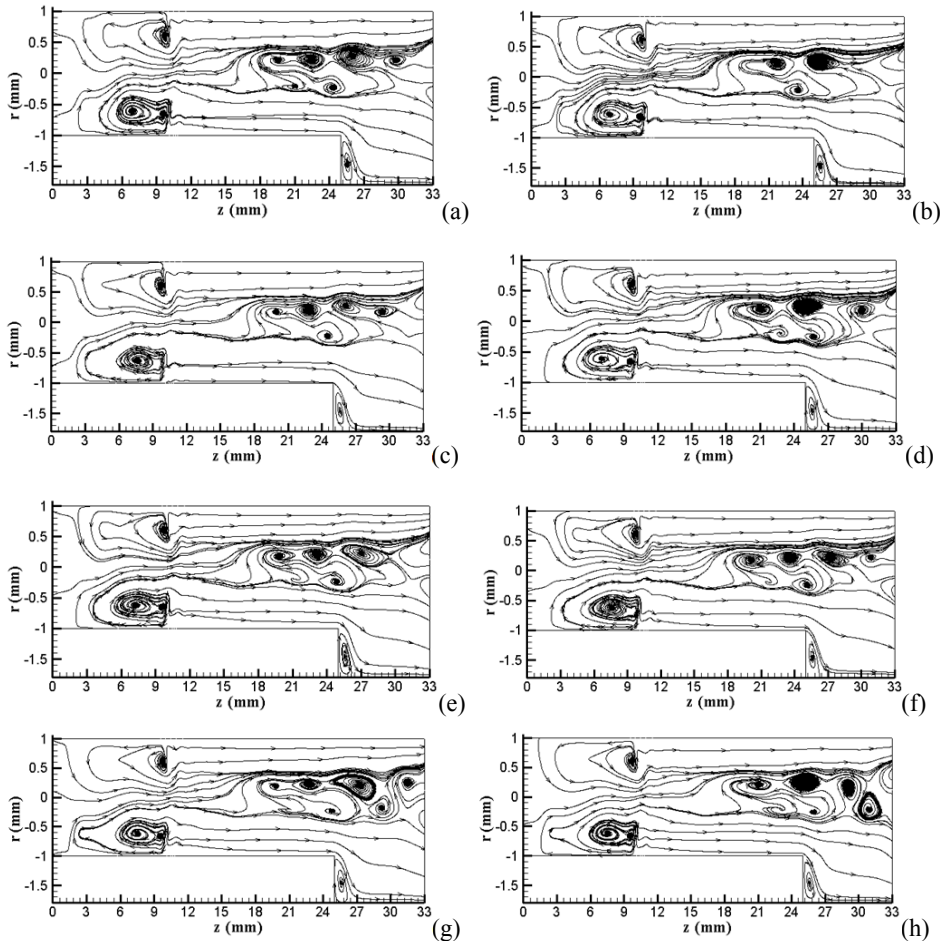


Figure 8: Time series of the streamlines in the  $y-z$  plane at  $x=0\text{mm}$  for a nozzle with five rectangular grooves (Case 3): (a)  $t=1.1 \times 10^{-3}\text{s}$ ; (b)  $t=1.13 \times 10^{-3}\text{s}$ ; (c)  $t=1.15 \times 10^{-3}\text{s}$ ; (d)  $t=1.16 \times 10^{-3}\text{s}$ ; (e)  $t=1.18 \times 10^{-3}\text{s}$ ; (f)  $t=1.22 \times 10^{-3}\text{s}$ ; (g)  $t=2.18 \times 10^{-3}\text{s}$ ; (h)  $t=2.2 \times 10^{-3}\text{s}$

( $n=3, 5$ ), and the recirculation zone increases in the axial direction as the groove height increases. Hence, the recirculation zones in case 2 ( $n=4$ ) are the largest and the smallest in case 1 ( $n=3$ ). It is observed from the figures that the air upstream of the injector rotates in the opposite direction to that in the injector downstream (streamlines at  $x=0.4\text{mm}$  plane in Fig. 9). The occurrence of the opposite rotation in case 2 is the earliest as compared with other cases. For the corner recircula-

tion zone (CRZ), the recirculation length increases with increase in groove number. The streamlines in the twisting chamber of the cross sections (in the  $x - y$  plane at  $z=26\text{mm}$ ) are smooth. The center of the large swirling flow is on  $z$ -axis, which leads to a zero radial and azimuthal velocity component at the axis. It is noteworthy that there are air currents in mutually opposite direction in the grooves and the twisting chamber. This is because a backward-facing step flow is formed due to the grooves. For all cases, the large vortex rings (recirculation zone) in the grooves are similar.

## 5 Conclusions

In the present paper, the 3D compressible swirling recirculating flow in a nozzle with a slotted-tube has been studied together with a simulated observation on the effect of the groove number on the flow pattern. Qualitative agreements between the model predictions and experimental results on streamline angles are achieved. The following conclusions can be drawn after the detailed analysis:

1. There are three recirculating zones which are near the upstream wall of the injectors, in the downstream center of the injectors and behind the step of the grooves, respectively.
2. For all cases under study, as the sizes of recirculating zones near upstream wall and behind the steps are almost constant, the spiral breakdown in downstream of the injectors shows a periodic development. Much longer computing time is needed to have a periodic solution as the groove number increases. Contrary to the results of the case 3 ( $n=5$ ), the fluid gradually decays over time for cases 1 and 2 ( $n=3, 4$ ).
3. Owing to geometry symmetry, for case 2 ( $n=4$ ), the vortex breakdown occurs earlier with axis, and the size and strength of the vortices are larger compared with that in two other cases ( $n=3, 5$ ). Again, the location of the breakdown point moves downward over time in case 2. However, the breakdown points seem to be “frozen” in at the same position for cases 1 and 3.

**Acknowledgement:** The authors wish to acknowledge the funding support from the Hong Kong Polytechnic University for the work reported here.

## References

**Benim, C.; Nahavandi, A.** (2003): A computational analysis of turbulent swirling flows. *Turbulence, Heat and Mass Transfer 4*. Begell House, New York, pp.715-722.

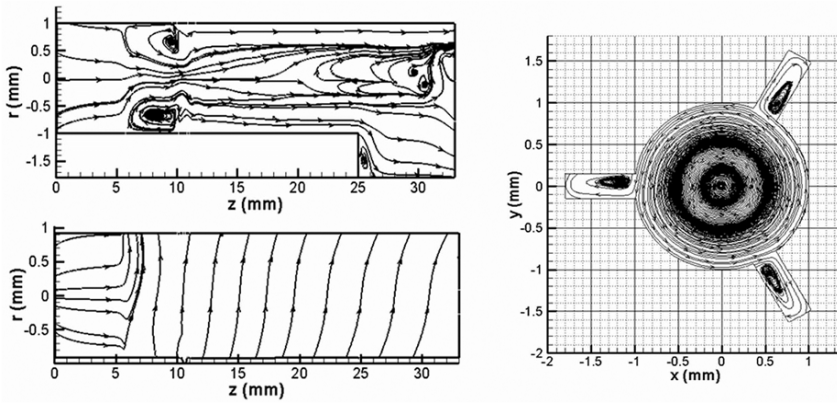
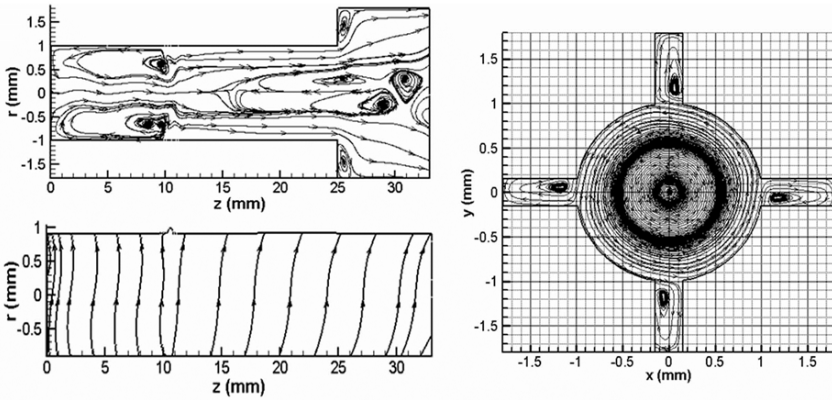
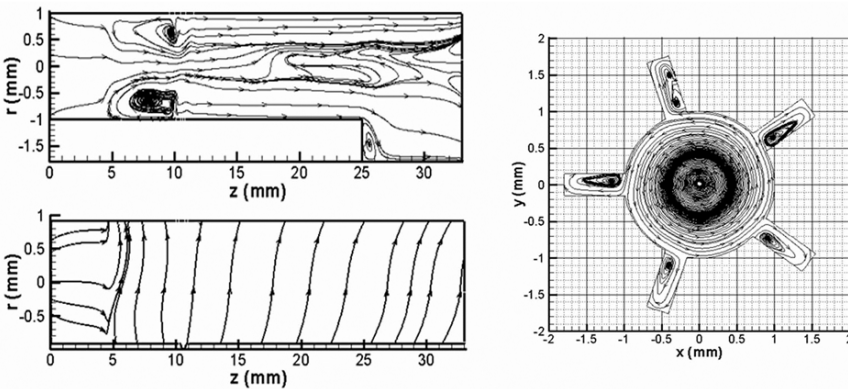
(a) Case 1, groove number  $n = 3$ (b) Case 2, groove number  $n = 4$ (c) Case 3, groove number  $n = 5$ 

Figure 9: The steady state streamline plots at three sections for different groove number. For every case: left-up figure, the  $y-z$  plane at  $x=0\text{mm}$ ; left-down figure, the  $y-z$  plane at  $x=0.4\text{mm}$ ; right figure, the  $x-y$  plane at  $z=26\text{mm}$ .

- Benim, C; Nahavandi, A; Syed K.J.** (2005): T-RANS based analysis of turbulent swirling flows. *Computational Fluid and Solid Mechanics, Elsevier*, pp.590-593.
- Brücker, Ch.** (1993): Study of vortex breakdown by particle tracking velocimetry, Part 2: spiral-type vortex breakdown. *Exp. Fluids*, vol.14, pp.133-139.
- Brücker, Ch; Althaus, W.** (1995): Study of vortex breakdown by particle tracking velocimetry (PTV), Part 3: time-dependent structure and development of breakdown-modes. *Exp. Fluids*, vol.18, pp.174-186.
- Chang, F.; Dhir, V.K.** (1994): Turbulent flow field in tangentially injected swirl flows in tubes. *Int. J. Heat Fluid Flow*, vol.15, no.5, pp. 346-356.
- Chang, K.C.; Chen, C.S.** (1993): Development of a hybrid  $k-\epsilon$  turbulence model for swirling recirculating flows under moderate to strong swirl intensities. *Int. J. Numer. Methods Fluids*, vol.16, no.5, pp.421-443.
- Chang, T.H.** (2004): Experimental study on turbulent swirling flow in a cylindrical annuli by using the PIV technique. *Int. J. Automotive Technology*, vol.5, no.1, pp.17-22.
- Dellenback, P.S.; Metzger, D.E.; Neitzel, G.P.** (1988): Measurement in turbulent swirling flow through an abrupt axisymmetric expansion. *AIAA J.*, vol.26, no.6, pp.669-681.
- Escudier, M.** (1988): Vortex breakdown: observations and explanations. *Progress Aero. Sci.*, vol.25, no.2, pp.189-229.
- Escudier M.P.; Keller J.J.** (1985): Recirculation in swirling flow: a manifestation of vortex breakdown. *AIAA J.*, vol.23, no.1, pp.111-116.
- Favre, A.** (1969): Statistical equations of turbulent gases, Problems of Hydrodynamics and Continuum Mechanics. *Society for Industrial and Applied Mathematics (SIAM), Philadelphia*, pp.231-266.
- Freitag, M.; Klein, M.** (2005): Direct numerical simulation of a recirculating swirling flow. *Flow Turbul. Combust.*, vol.75, pp.51-66.
- Guo, H.F.; Chen, Z.Y.; Yu, C.W.** (2010): 3D tangentially injected swirling recirculating flow in a nozzle with a slotted-tube - effects of groove parameters. *Int. J. Numer. Methods Fluids*, vol.63, pp.1256-1269.
- Gupta, A.K.; Lilley, D.G.; Syred, N.** (1984): Swirl flows. *Abacus Press: Tunbridge Wells, U.K.*
- Hogg, S.; Leschziner, M.A.** (1989): Computation of highly swirling confined flow with a Reynolds stress turbulence model. *AIAA J.*, vol.27, no.1, pp.57-63.
- Kim, J.Y.; Ghaja, A.J.; Tang, C.; Foutch, G.L.** (2005): Comparison of near-wall treatment methods for high Reynolds number backward-facing step flow. *Int. J.*

*Computational Fluid Dynamics*, vol.19, no.7, 493–500.

**Kim, K.Y.; Chung, M.K.** (1987): New eddy viscosity model for computation of swirling turbulent flows. *AIAA J.*, vol.25, no.7, pp.1020-1022.

**Kim, S.E.; Choudhury, D.** (1995): A near-wall treatment using wall functions sensitized to pressure gradient. *ASME FED Separated Complex Flows*, vol.217, pp. 273-279.

**Kitoh O.** (1991): Experimental study of turbulent swirling flow in a straight pipe. *J. Fluid Mech.*, vol.225, pp.445–47.

**Launder, B.E.; Spalding, D.B.** (1974): The numerical computation of turbulent flows. *Comput. Methods Appl. Mech. Eng.*, vol. 3, pp. 269–289.

**Leonard, B.P.; Mokhtari, S.** (1990): Ultra-sharp nonoscillatory convection schemes for high-speed steady multidimensional flow. *NASA technical memorandum 102568 (ICOMP-90-12)*, NASA Lewis Research Center.

**Nagendra, D.** (2001): Numerical simulations of an isothermal confined swirling jet in a dump combustor. Retrieved, from the World Wide Web: <https://engineering.purdue.edu>.

**Nallasamy, M.** (1987): Turbulence models and their applications to the prediction of internal flows: a review. *Comput Fluids*, vol.15, no.2, pp.151-194.

**Nejad, S.; Ahmed, S.A.** (1992): Flow field characteristics of an axisymmetric sudden-expansion pipe flow with different initial swirl distribution. *Int. J. Heat Fluid Flow*, vol.13, no.4, pp.314-321.

**Sarpkaya, T.** (1971): On stationary and travelling vortex breakdowns. *J. Fluid Mech.*, vol.45, pp.545-559.

**Settles, G.S.; Teng, H.Y.** (1983): Flow visualization methods for separated three-dimensional shock wave/turbulent boundary-layer interactions. *AIAA J.*, vol.21, no.3, pp.390-397.

**Sharif M.A.R.; Wong Y.K.E.** (1995): Evaluation of the performance of three turbulence closure models in the prediction of confined swirling flow. *Comput. Fluids*, vol.24, no.1, pp.81-100.

**Shih, T.H.; Liou, W.W.; Shabbir, A.; Zhu, J.** (1995): A new  $k-\varepsilon$  eddy-viscosity model for high Reynolds number turbulent flows. *Comput. Fluids*, vol. 24, no.3, pp.227-238.

**Shore, N.A.; Haynes, B.S.; Fletcher, D.F.; Sola, A.A.** (1996): Numerical aspects of swirl flow computation. *Proc. CTAC95, Melbourne, Australia, July 3-5, 1995*, pp. 693-700.

**Sparrow, E.M.; Chaboki, A.** (1984): Swirl-affected turbulent fluid flow and heat transfer in a circular tube. *ASME J. Heat Transfer*, vol.106, pp.766-773.

**Steenbergen, W.** (1995): *Turbulent Pipe Flow with Swirl*. Ph.D. thesis, Eindhoven University of Technology.

**Steenbergen W.; Voskamp J.** (1998): The rate of decay of swirl in turbulent pipe flow. *Flow Meas. Instrum.*, vol. 9, pp.67–78.

**Wang, P.; Bai, X.S.; Wessman, M.; Klingmann, J.** (2004): Large eddy simulation and experimental studies of a confined turbulent swirling flow. *Phys. Fluids*, vol.16, no.9, pp. 3306-3324.

**Yajnik, K.S.; Subbaiah, M.V.** (1973): Experiments on swirling turbulent flows. Part 1: similarity in swirling flows. *J. Fluid Mech.*, vol. 60, pp.665–87.

